Analysis of hydrodynamic fluctuations in heterogeneous adjacent multidomains in shear flow

Xin Bian, Mingge Deng, Yu-Hang Tang, and George Em Karniadakis

Analysis of hydrodynamic fluctuations in heterogeneous adjacent multidomains in shear flow

Xin Bian,[*] Mingge Deng, Yu-Hang Tang, and George Em Karniadakis[†]

Division of Applied Mathematics, Brown University, Providence, Rhode Island 02912, USA

We analyze hydrodynamic fluctuations of a hybrid simulation under shear flow. The hybrid simulation is based on the Navier-Stokes (N-S) equations on one domain and Dissipative Particle Dynamics (DPD) on the other domain. The two domains overlap and there is an artificial boundary for each domain within the overlapping region. To impose the artificial boundary of the N-S solver, a simple spatial-temporal averaging is performed on the DPD simulation. In the artificial boundary of the particle simulation, four popular strategies of constraint dynamics are implemented, namely, the Maxwell buffer [Hadjiconstantinou and Patera, International Journal of Modern Physics C, 1997, 08, 967], the relaxation dynamics [O'Connell and Thompson, Physical Review E, 1995, 52, R5792], the least constraint dynamics [Nie et al, Journal of Fluid Mechanics, 2004, 500, 55; Werder et al, Journal of Computational Physics, 2005, 205, 373], and the flux imposition [Flekkøy et al, Europhysics Letters, 2000, 52, 271] to achieve a target mean value given by the N-S solver. Going beyond the mean flow field of the hybrid simulations, we investigate the hydrodynamic fluctuations in the DPD domain. To this end, we calculate the transversal autocorrelation functions of the fluctuating variables in k-space, to evaluate the generation, transport and dissipation of fluctuations in the presence of a hybrid interface. We quantify the unavoidable errors in the fluctuations, due to both the truncation of the domain and the constraint dynamics performed in the artificial boundary. Furthermore, we compare the four methods of constraint dynamics and demonstrate how to reduce the errors in fluctuations. The analysis and findings of this work are directly applicable to other hybrid simulations of fluid flow with thermal fluctuations.

PACS numbers: 47.11.St, 47.61.-k, 05.40.Ca, 05.20.Jj.

I. INTRODUCTION

Despite the recent advances in high performance computer simulations in multiscale fluid mechanics, a monolithic microscopic or mesoscopic simulation would be computationally prohibitive. On the contrary, a continuum-based simulation may be very efficient, but often lacks many details such as thermal fluctuations, accurate constitutive equations, and correct boundary conditions, to name but a few. Hence, a hybrid simulation, which combines the detailed dynamics of a fine model and the computational efficiency of a coarse model, seems to be a good candidate to simulate multiscale problems.

In the last two decades, many attempts have been made to couple two levels of descriptions for fluids [1–14]. In particular, the majority of the hybrid simulations follow the framework of the domain decomposition method (DDM) with two overlapping subdomains [15]. In each subdomain, a different solver is selected in conjunction with an artificial boundary within the overlapping region. With time advancing, each artificial boundary is updated by the interior values of the other subdomain and the computation proceeds in each subdomain, alternatively. The quantity of interest has been often the *mean field* variables, such as velocity, density, and stress, which are sufficient from the continuum perspective. Surprisingly, the corresponding thermal fluctuations were simply con-

sidered as unwanted noises to be filtered out. However, the thermal fluctuations are one of the most prominent features at micro- and meso-scales and in some cases the driving mechanism for the dynamics of colloids, polymers and biological cells [16–22]. Simply filtering out the fluctuations would ignore a large portion of the physics unique to micro- and meso-scales. There are a few works, where thermal fluctuations were indeed allowed to propagate through the hybrid interface [7, 8]. Nevertheless, a quantitative method of analyzing the thermal fluctuations is still lacking and we do not know if the fluctuations are accurately reproduced in the presence of a hybrid interface.

In this work, we analyze some of the previously proposed methods and focus primarily on the thermal fluctuations. To this end, we consider hybrid simulations of a simple shear flow, where the flow in one subdomain is described by a N-S solver using a finite difference method (FDM). On the other subdomain we employ a mesoscopic dissipative particle dynamics (DPD) solver. In the overlapping region, we select four methods for the constraint dynamics in the artificial boundary of the DPD simulation. They are the Maxwell buffer [2], the relaxation dynamics [1], the least constraint dynamics [4, 5] and the flux imposition [3, 8] methods. To date, there has not been a consensus as to which of the four methods is most effective, as they are all capable of generating accurate mean profiles.

To quantify the error in thermal fluctuations, we calculate the transversal autocorrelation functions (TACFs) of the fluctuating variables in k-space, that is, the spa-

---

tial Fourier transform of the fluctuations. The TACFs indicate if the fluctuations are generated, transported and dissipated correctly [23, 24]. In a periodic shear flow, the TACFs can be obtained analytically by solving the linearized fluctuating hydrodynamics [25]. Firstly, we compare the TACFS of DPD simulations with the theory in Lees-Edwards boundary conditions [26]. Subsequently, in wall-bounded shear flow, we examine the TACFs of hybrid simulations by taking the results of full DPD simulations as reference. We compare the errors of the TACFs among the four methods of constraint dynamics quantitatively and also discuss how to reduce the errors in thermal fluctuations in the hybrid simulations. The same analysis is applicable to other methods of concurrent coupling, such as one between a continuum solver and a molecular dynamics with the Lennard-Jones potential. This study on simple fluid is also a fundamental step towards evaluating various coupling algorithms in a more complex fluid, involving soft matter whose dynamics depends strongly on thermal fluctuations and related correlations.

The rest of the paper is organized as follows. In Section II, we introduce briefly the DPD and FDM methods, and further explain some details about the concurrent coupling of the two methods. Some conceptual comparisons are made and mean flow profiles of hybrid simulations are obtained. In Section III, analytical expressions for TACFs under periodic shear flow are given and validated by DPD simulations. Furthermore, in wall-bounded shear flows, TACFs from hybrid simulations and full DPD simulations are compared in detail and errors in fluctuations from hybrid simulations are quantified. In particular, sources of errors in the fluctuations are identified. In Section IV, we summarize our findings. Further details about boundary conditions in particle simulations are given in Appendix A.

II. THE MULTISCALE MODEL

We follow the framework of the DDM [15], which enables coupling of two solvers of partial differential equations. Similarly, we couple two heterogeneous fluid solvers in two subdomains with an overlapping region, as sketched in Fig. 1. In one subdomain, we select the DPD method as the mesoscopic solver. In the other subdomain, we have the FDM as the continuum solver. Next, we shall describe the two methods and elaborate on the details of the coupling, especially the four methods of implementing the constraint dynamics in the artificial boundary of the particle simulation.
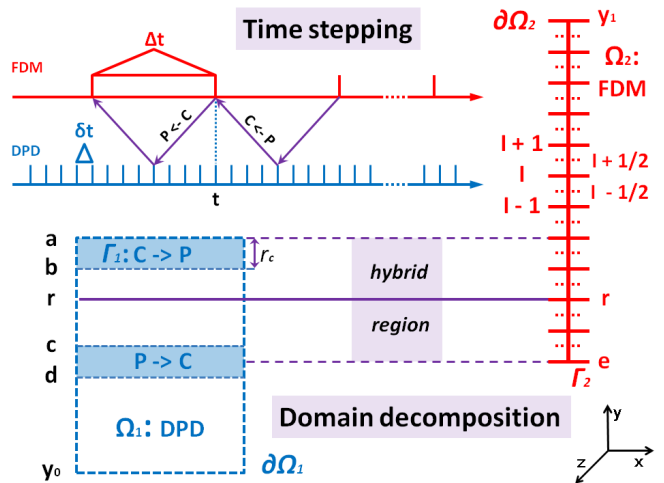

FIG. 1: (Color online) Sketch of the domain decomposition method and time stepping. The left-top part of the figure is about time stepping while the right-bottom part is about decomposition of the simulation domain. Subdomain Ω_1 is described by a dissipative particle dynamics (DPD) simulation, while subdomain Ω_2 is described by a finite different method (FDM). The whole domain is bounded by two no-slip walls $\partial\Omega_1$ and $\partial\Omega_2$, at $y = y_0$ and y_1, respectively. An artificial boundary $\Gamma_1 : [y_b, y_a]$ applies to the DPD and an artificial boundary $\Gamma_2 : y = y_e$ applies to the FDM. A hybrid reference line is defined at $y = y_r$, at which the global solution is pieced together by combining results from DPD below y_r and results from FDM above y_r. FDM runs with time step Δt and DPD runs with time step δt, where $\Delta t = N_s \delta t$ and N_s is a positive integer. Time integrations of FDM and DPD are staggered. The arrows between two time axes indicate information passing. The communication time step between the two simulations is $\Delta t_{comm} = \Delta t$.

A. Dissipative particle dynamics (DPD)

For convenience, as reference we define some simple notations

$$\mathbf{r}_{ij} = \mathbf{r}_i - \mathbf{r}_j,$$
$$\mathbf{v}_{ij} = \mathbf{v}_i - \mathbf{v}_j,$$
$$\mathbf{e}_{ij} = \mathbf{r}_{ij}/r_{ij}, \quad r_{ij} = |\mathbf{r}_{ij}|, \tag{1}$$

where $\mathbf{r}_i$, $\mathbf{v}_i$ are position and velocity of particle i; $\mathbf{r}_{ij}$, $\mathbf{v}_{ij}$ are relative position and velocity of particles i and j; r_{ij} is the distance of the two and $\mathbf{e}_{ij}$ is the unit vector pointing j to i. We consider the classical DPD method, which has three pairwise forces described as follows [27–29],

$$\mathbf{F}_{ij}^C = aW^C(r_{ij})\mathbf{e}_{ij}, \tag{2}$$
$$\mathbf{F}_{ij}^D = -\gamma W^D(r_{ij})(\mathbf{e}_{ij} \cdot \mathbf{v}_{ij})\mathbf{e}_{ij}, \tag{3}$$
$$\mathbf{F}_{ij}^R = \sigma W^R(r_{ij})\theta_{ij}\mathbf{e}_{ij}\delta t^{-1/2}, \tag{4}$$

where coefficients a, γ, and σ reflect the strength of individual forces; W^C, W^D, and W^R are weighting functions that monotonically decay with relative distance r_{ij}; $\theta_{ij} = \theta_{ji}$ is a Gaussian white noise with

$$< \theta_{ij}(t) > = 0, \tag{5}$$
$$< \theta_{ij}(t)\theta_{kl}(t') > = (\delta_{ik}\delta_{jl} + \delta_{il}\delta_{jk})\,\delta(t-t'), \tag{6}$$

where δ_{ij} is the Kronecker δ and $\delta(t-t')$ is the Dirac δ function. The DPD version of the fluctuation-dissipation theorem reads as

$$W^D(r_{ij}) = \left[W^R(r_{ij})\right]^2, \tag{7}$$
$$2k_B T\gamma = \sigma^2, \tag{8}$$

which warrants the Gibbs canonical ensemble [28]. A typical form of the weighting kernel is suggested as [28–30]

$$W^{C,R}(r_{ij}) = \begin{cases} (1 - r_{ij}/r_c)^k, & r_{ij} < r_c, \\ 0, & r_{ij} \geq r_c. \end{cases} \tag{9}$$

Following Ref. [31], we take $a = 25.0$, $\sigma = 3.0$, $\gamma = 4.5$, $r_c = 1$ and $k_B T = 1.0$; $k = 1$ for W^C and $k = 0.25$ for W^R; particle mass $m = 1$, number density $n = 3.0$ and mass density $\rho = mn = 3.0$. For this particular set of input parameters, the kinematic viscosity of the fluid measures as $\nu = 0.54$ in DPD units. The velocity Verlet time integrator is employed [24, 29] and $\delta t = 0.005$. At equilibrium, the relaxation time of DPD is about $180\delta t$, after which the velocity autocorrelation function of particles decays below 1.5%.

B. Finite difference method (FDM)

Since we wish to focus on the thermal fluctuations, a simple shear flow is sufficient as a test-bed. Therefore, in the continuum case the momentum equation reduces to be one dimensional as

$$\rho\frac{\partial V^x}{\partial t} = \frac{\partial \tau^{xy}}{\partial y}, \tag{10}$$
$$\tau^{xy} = \eta\frac{\partial V^x}{\partial y}, \tag{11}$$

where the flow is along the x direction and the velocity gradient is along the y direction. The velocity of the continuum is capitalized to distinguish it from that of the particle simulation. We implement a one dimensional FDM along y, where the velocity is defined at each grid point indexed by integer I and the stress is defined in the middle between each two neighboring grid points, as sketched on the right side of Fig. 1. For time integration, we choose a forward-Euler scheme. Therefore, we have

$$\rho\frac{V_I^x(t+\Delta t) - V_I^x(\Delta t)}{\Delta t} = \frac{\tau_{I+1/2}^{xy} - \tau_{I-1/2}^{xy}}{\Delta y}, \tag{12}$$
$$\tau_{I-1/2}^{xy} = \eta\frac{V_I^x - V_{I-1}^x}{\Delta y}, \tag{13}$$
$$\tau_{I+1/2}^{xy} = \eta\frac{V_{I+1}^x - V_I^x}{\Delta y}, \tag{14}$$

with dynamic viscosity $\eta = \nu\rho$ and time step $\Delta t \leq \frac{\Delta y^2}{2\nu}$ for stability. The dynamic viscosity and density are $\eta = 1.62$ and $\rho = 3.0$, respectively, consistent with the particle simulation. We take $\Delta y = 1$ and $\Delta t = 0.9$, which satisfies the stability condition while is still no less than the relaxation time of the particle dynamics, that is, $\Delta t = N_s\delta t = 180\delta t$. All the values in the FDM are also expressed in the DPD units.

C. Concurrent coupling between particle dynamics and continuum description

For a hybrid simulation, the coupling is done along the y direction, as indicated in Fig. 1. The hybrid reference line is fixed at $y_r = 10$ and the global solution combines the solution of the particle simulation below y_r and the solution of the continuum above y_r. The subdomain of DPD spans $[0, 10] \times [0, 10]$ in x and z direction. In y direction, it ranges from $y_0 = 0$ to y_a. In a wall-bounded domain, there is a wall boundary $\partial\Omega_1$ with the no-slip condition applied at $y = y_0$. Technical details on boundary conditions of DPD are given in Appendix A. An artificial boundary Γ_1 for particle dynamics is located at $y_b \leq y < y_a$ and its size is fixed as $y_a - y_b = r_c = 1$. The default location of Γ_1 is between $y_b = y_r = 10$ and $y_a = 11$, and we shall study its effects at different locations on the results in Section III B. The one dimensional FDM ranges from $y_e = 8$ to $y_1 = 30$ in y direction. No-slip condition applies at y_1 and the artificial boundary Γ_2 for the velocity is located at y_e.

The time integrations of the two simulations are staggered. To minimize the lag time of information exchange [11], we take $\Delta t_{comm} = \Delta t = 180\delta t$. More specifically, the particle simulation integrates with time step δt from $t = t - 3\Delta t/2$ to $t = t - \Delta t/2$. To impose the artificial boundary Γ_2 for the continuum ($P \to C$) at $t - \Delta t$, it is straightforward to perform simple spatial averaging on particle velocities between $y_d \leq y < y_c$, and thereafter temporal averaging over $t - 3\Delta t/2 < t \leq t - \Delta t/2$ as

$$V_e = \frac{1}{N_s}\sum_{j=1}^{N_s}\frac{1}{N_{cd}}\sum_{i=1}^{N_{cd}} v_i. \tag{15}$$

Here, N_{cd} is the instantaneous number of particles located in cell $P \to C$ and $N_s = \Delta t/\delta t = 180$. Furthermore, the region $P \to C$ is centered at y_e with a thickness of $r_c = 1$, therefore, $y_c = 8.5$ and $y_d = 7.5$.

Once V_e is updated at $t - \Delta t$, the FDM integrates one step from $t - \Delta t$ to t. Its new solutions V_a and V_b at y_a and y_b, respectively, are passed to particle simulations and are further utilized in various ways (by the constraint dynamics as explained later) to set the artificial boundary Γ_1 of the particle simulation from $t - \Delta t/2$ to $t + \Delta t/2$. Meanwhile, the DPD simulation integrates with time step δt from $t - \Delta t/2$ to $t + \Delta t/2$. Afterwards, again Eq. (15) is applied to impose V_e of Γ_2 at t. The alternation of imposing artificial boundaries and

the staggered integrations of the two simulations repeat until the end of the hybrid simulation.

Due to the truncation of the subdomain for the DPD simulation, an average pressure must be imposed on the truncation line $y = y_a$ inwards. We follow Refs. [5, 31] to calculate an average conservative force $\mathbf{F}^C_{ave}(y_i)$, which reflects the effects outside y_a in the continuum limit. $\mathbf{F}^C_{ave}(y_i)$ is position-dependent and applies to particles with $y_a - y_i < r_c$ distance from y_a in the interior, that is, particles in Γ_1. Technical details on calculating $\mathbf{F}^C_{ave}(y_i)$ are given in Appendix A. This approach proves to induce negligible density oscillations near the boundary [5, 31]. The imposed $\mathbf{F}^C_{ave}(y_i)$ is an averaged force and does not completely prevent particles from leaving to outside. Hence, we further apply a specular reflection at y_a if a particle goes outside of y_a. We note that $\mathbf{F}^C_{ave}(y_i)$ and the specular reflection at y_a are associated with the truncation of the particle subdomain.

There is *no unique way* to impose the artificial boundary in Γ_1 ($C \rightarrow P$) from $t - \Delta t/2$ to $t + \Delta t/2$, as many extra degrees of freedom on particles are underdetermined. The usual strategy is to perform a constraint dynamics on each particle i in Γ_1 in such a way that

$$\frac{1}{N_{\Gamma_1}} \sum_{i=1}^{N_{\Gamma_1}} v_i = \overline{V}_{\Gamma_1}, \qquad (16)$$

is satisfied at every δt or on average over $N_s \delta t$ and thermal fluctuations are affected as little as possible. Here, N_{Γ_1} is the instantaneous number of particles in Γ_1 and $\overline{V}_{\Gamma_1}$ is the average velocity of the continuum solutions in the same region. In this case, $\overline{V}_{\Gamma_1} = (V_a + V_b)/2$ at time t.

In the following, we will employ four methods of constraint dynamics in Γ_1. Since we deal primarily with one-dimensional shear flow, we use scalar variables instead of vector ones. The constraint of the particle dynamics is always performed in x direction of the flow, and therefore the index for x is omitted. Velocities in y and z directions are not altered by the constraint dynamics.

1. Maxwell buffer

The Maxwell buffer was first proposed in Ref. [2] as

$$v_i = V_i + \delta v_i, \qquad (17)$$
$$V_i = V_b + (V_a - V_b)(y_i - y_b)/\Delta y, \qquad (18)$$

where a deterministic component V_i is obtained by a linear interpolation between the values on the two nearest grid points V_a and V_b. Under the assumption of a local equilibrium for DPD, the stochastic component δv_i is drawn from a Maxwell-Boltzmann distribution at a given temperature $k_B T = 1$,

$$p(\delta v_i) = \sqrt{\frac{m}{2\pi k_B T}} exp\left[\frac{-m(\delta v_i)^2}{2k_B T}\right]. \qquad (19)$$

It is simple to see that Eqs. (17) and (18) satisfy directly the constraint posed in Eq. (16). Moreover, the x components of the usual interacting forces $\mathbf{F}^C_{ij}$, $\mathbf{F}^D_{ij}$ and $\mathbf{F}^R_{ij}$ are completely ignored for updating the velocities of particles in Γ_1.

2. Relaxation dynamics

A relaxation dynamics method was proposed in the first paper of hybrid simulations on liquid flow as [1],

$$\dot{v}_i = \frac{F_i}{m} + \frac{\epsilon}{\delta t}\left(\overline{V}_{\Gamma_1} - \frac{1}{N_{\Gamma_1}}\sum_{j=1}^{N_{\Gamma_1}} v_j\right), \qquad (20)$$

where F_i is the usual total particle force on particle i. The rest of the terms on the right hand side act as a relaxing force, which drives each particle i in Γ_1 towards the average velocity $\overline{V}_{\Gamma_1}$ over $\delta t/\epsilon$ time period. In Ref. [1], the continuum has the same time step as that of the particle simulation, that is, $\Delta t = \delta t$. Moreover, the relaxation parameter is chosen as $\epsilon = 0.01$ for the particular properties of the fluid simulated in Ref. [1], where the authors argue that a smaller value of ϵ provides inadequate coupling while a larger value may lead to excessive damping of thermal fluctuations.

3. Principle of least constraint

By taking the extremum of the time integral of the Lagrangian for the particles in Γ_1, which is subject to the non-holonomic constraint in Eq. (16), the equation of motion (EoM) for each particle i in Γ_1 is according to Ref. [4]

$$\dot{v}_i = \frac{F_i}{m} - \frac{1}{N_{\Gamma_1}}\sum_{j=1}^{N_{\Gamma_1}} \frac{F_j}{m} + \frac{1}{\delta t}\left(\overline{V}_{\Gamma_1} - \frac{1}{N_{\Gamma_1}}\sum_{j=1}^{N_{\Gamma_1}} v_j\right) \quad (21)$$

Instead of repeating the derivation for Eq. (21) as in Ref. [4], we may arrive at the same expression from another perspective. To satisfy the constraint in Eq. (16), an extra body force $F^b_{\Gamma_1}$ is introduced *dynamically* at every time step δt such that [5]

$$\overline{v}'_{\Gamma_1} = \overline{v}_{\Gamma_1} + \frac{\delta t}{N_{\Gamma_1} m}(F_{\Gamma_1} + F^b_{\Gamma_1}), \qquad (22)$$

where $\overline{v}_{\Gamma_1}$ is the average velocity and F_{Γ_1} is the total force in Γ_1 due to particle interactions,

$$\overline{v}_{\Gamma_1} = \frac{1}{N_{\Gamma_1}}\sum_{j=1}^{N_{\Gamma_1}} v_j, \qquad (23)$$

$$F_{\Gamma_1} = \sum_{i=1}^{N_{\Gamma_1}} F_j. \qquad (24)$$

To satisfy Eq. (16), we set $\overline{v}'_{\Gamma_1} = \overline{V}_{\Gamma_1}$, and therefore, we obtain an expression for the body force $F^b_{\Gamma_1}$ as

$$F^b_{\Gamma_1} = \frac{N_{\Gamma_1} m}{\delta t}(\overline{V}_{\Gamma_1} - \overline{v}_{\Gamma_1}) - F_{\Gamma_1},$$

$$= \frac{N_{\Gamma_1} m}{\delta t}(\overline{V}_{\Gamma_1} - \frac{1}{N_{\Gamma_1}}\sum_{j=1}^{N_{\Gamma_1}} v_j) - \sum_{j=1}^{N_{\Gamma_1}} F_j. \quad (25)$$

The value of $F^b_{\Gamma_1}$ is dynamic and may vary at every δt. If we spread the body force $F^b_{\Gamma_1}$ from Eq. (25) *evenly* on N_{Γ_1} particles in Γ_1, it gives exactly the same EoM as in Eq. (21) for each particle i.

4. Imposition of flux

The exchange of flux for dense fluids was first proposed in Ref. [3]. Rather than constraining the state variables directly, as done in the previous three methods, this method imposes flux at the truncation line y_a of the subdomain of particle simulation. Therefore, the EoM of particles in Γ_1 reads

$$\dot{v}_i = \frac{F_i}{m} + F^x(y_i), \quad (26)$$

$$F^x(y_i) = \tau_a^{xy} A \lambda(y_i), \quad (27)$$

where $A = L_x \times L_z$ is the surface area of the truncation and τ_a^{xy} is the shear stress at y_a from the continuum. The distribution function $\lambda(y_i)$ of the shear force on each particle must be normalized

$$\lambda(y_i) = g(y_i) / \sum_{j=1}^{N_{\Gamma_1}} g(y_j), \quad (28)$$

where $g(y)$ is an arbitrary function so that $\lambda(y)$ diverges at $y = y_a$ and decays to zero as y approaches y_b from y_a.

If we assume that there is a locally linear shear flow within Γ_1, which is a reasonable assumption for many flow problems, then the distribution function $\lambda(y)$ may be defined better than an arbitrary one [32]. By assuming a locally linear shear flow, we can work out the continuum limit of the shear forces on line y_a from particles within Γ_1. By setting the shear force on y_a from particles equal to the continuum solution of FDM at y_a, we have an identity as follows

$$A\tau_a^{xy} = \int_0^{r_c} A d\gamma^D(h) h \dot{\gamma} dh, \quad (29)$$

where h is the distance of particle i from y_a ($h = y_a - y_i$), and $\dot{\gamma}$ is an arbitrary shear rate, while $\gamma^D(h)$ has the same expression as that of the averaged dissipative force from the exterior of an interface, as given in Appendix A. Eq. (29) holds for an arbitrary shear rate $\dot{\gamma}$. Therefore, given a shear stress τ^{xy} from the continuum solution of FDM, the distribution of shear force on each particle i is independent of $\dot{\gamma}$ as

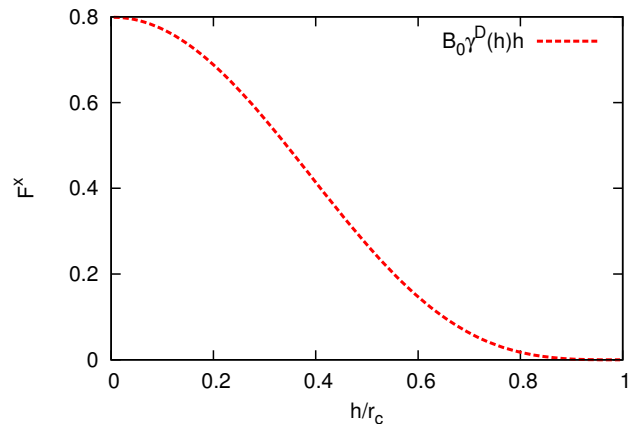$$F^x(y_i) = B_0 \tau_a^{xy} \gamma^D(h) h, \quad (30)$$

FIG. 2: Position-dependent shear force F^x on a DPD particle from the constraint dynamics of flux-imposition: h is the distance of a DPD particle from the truncation line y_a (see Fig. 1) and the quantity of F^x is for one unit of shear stress τ_a^{xy} given by the FDM solution.

where $B_0 = 0.776$ is a normalization constant for the particular DPD fluid considered. For one unit of shear stress τ_a^{xy}, the distribution function of shear force on particles in Γ_1 is illustrated in Fig. 2. We note that the implementation here resembles the flux boundary condition in Ref. [33].

5. Some remarks on different methods of constraint dynamics

The Maxwell buffer in Eq. (17) does not consider any inherent fluctuations of particles in Γ_1 and it simply shuffles the velocity of particles according to a Gaussian distribution. In this sense, it is the "strongest" constraint among others.

The approaches of relaxation and least constraint dynamics in Eqs. (20) and (21) are very similar ideas. The prominent feature of the relaxation dynamics is that it does not exclude the total net acceleration $\sum_{i=1}^{N_{\Gamma_1}} F_i/(N_{\Gamma_1} m)$ in Γ_1, whereas it has a flexible parameter ϵ to achieve both the targeted mean and little perturbations to the fluctuations. However, the choice of ϵ may cause practical difficulties. For different fluids and flow conditions, ϵ has to be tuned by trial simulations. In the hybrid simulations shown later, we have $\Delta t = 180\delta t$ and ϵ is tuned to be 0.02 to satisfy Eq. (16) best over $180\delta t$. In contrast, the approach in Eq. (21) applies the principle of least constraint in classical mechanics [34] to solve the non-holonomic constraint problem of Eq. (16) at every δt. Its practical implementation is very straightforward. Neither the relaxation dynamics nor the least constraint dynamics differentiates operations on individual particle i within the artificial boundary Γ_1.

The motivation of flux exchange is more fundamental

than that of the other three methods. The former considers the conservation of flux across the truncation line of the subdomain while the other three consider the matching of state variables (e.g. velocity) of the two solvers. The flux-exchange method does not require the two fluids from the two subdomains to be identical. Therefore, two fluids may have different properties, such as viscosities. In this work, we focus on the fluctuations of particle dynamics, therefore, we have two identical fluids and use the flux boundary only on particle simulations $(C \to P)$. The artificial boundary for the continuum $(P \to C)$ is achieved always by matching the state variables as in Eq. (15).

D. Mean flow profiles of hybrid simulations

We perform four sets of hybrid simulations for wall-bounded shear flow, where each of the four methods on constraint dynamics is applied on the artificial boundary Γ_1 of particle simulations. The bottom wall is held still and the upper wall moves with $v_w = 3$. The total box length is $L_y = 30$ in the y direction, therefore, $\dot{\gamma} = 0.1$. We show two examples of transient velocity profiles in Fig. 3, where particles on Γ_1 are constrained by the relaxation dynamics and flux imposition methods. The relaxation parameter in the former is tuned to be $\epsilon = 0.02$. For each velocity profile at time t, the finite difference solution is taken directly at t while the DPD solutions are average over $180\delta t$ between $t - \Delta t/2$ and $t + \Delta t/2$. The error bars indicate standard deviation of 20 individual and identical hybrid simulations. The error is small due to the large number of particles in $3D$ particle simulation for this $1D$ flow problem. Both the relaxation dynamics and flux imposition couple particle simulations well together with continuum with regard to the mean profiles. The methods of Maxwell buffer and least constraint dynamics achieve very similar accuracy so we do not show the results here.

We wish to examine the influence of the four methods of constraint dynamics on the hydrodynamic fluctuations in the hybrid simulations. Therefore, we shall briefly introduce the theory on fluctuation correlations.

III. TRANSVERSAL AUTOCORRELATION FUNCTIONS OF FLUCTUATIONS IN SHEAR FLOW

At equilibrium, it is well known that the correlation functions (CFs) of hydrodynamic fluctuations in k-space (spatial Fourier transform) encode the generation, transport, and dissipation of fluctuations [23, 24]. Analytical solutions of the linearized fluctuating hydrodynamics are also available to validate the results of particle simulations. Previously, it has been shown that (smoothed) dissipative particle dynamics (DPD) simulations can reproduce accurately various CFs [13]. At nonequilibrium,
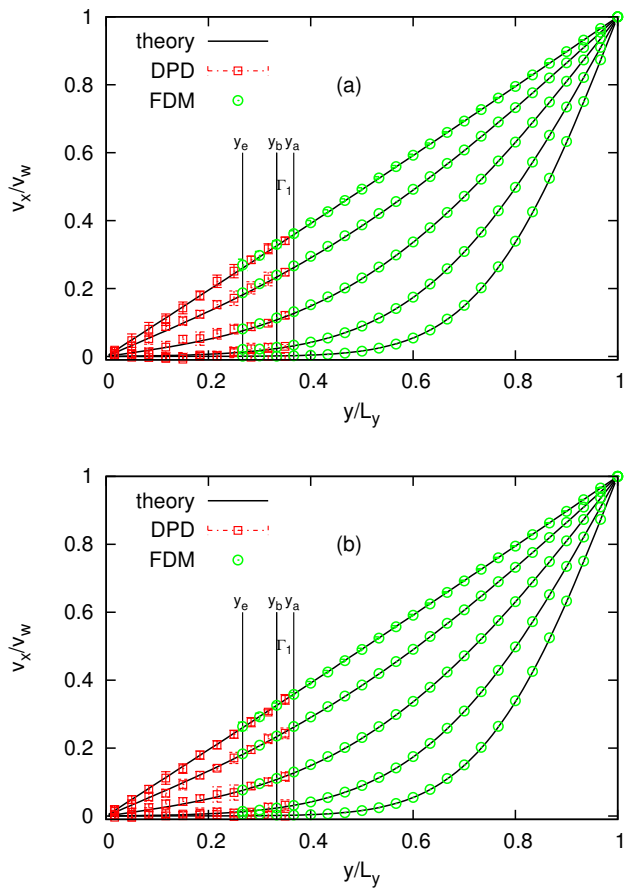

FIG. 3: (Color online) Velocity profiles of transient Couette flow by hybrid simulations of DPD coupled with FDM. (a) Relaxation dynamics with $\epsilon = 0.02$. (b) Imposition of flux. Data from bottom to top are according to $t = 36, 72, 144, 288$ and 720, respectively.

the CFs of hydrodynamic fluctuations may also be solved analytically for the steady state of periodic shear flow. We revisit some analytical results and give references for the detailed derivations. In particular, we focus on the transversal autocorrelation functions (TACFs), which are completely characterized by the shear mode and shear rate.

Suppose we have a simple shear flow in the x direction, the velocity gradient is along the y direction, and the vorticity is along the z direction; the shear rate is $\dot{\gamma}$. The usual periodic boundary conditions apply in the x and z directions while periodic boxes along the y direction shift $\pm L_y \dot{\gamma} t$, above and below the principal box, respectively. Therefore, if a particle crosses $y = L_y/2$ to outside, it enters the principal box again at $y = -L_y/2$ with x shifted $-L_y \dot{\gamma} t$, and v_x shifted by $-L_y \dot{\gamma}$; if the particle crosses $y = -L_y/2$ to outside, it enters the principal box again at $y = L_y/2$ with x shifted $L_y \dot{\gamma} t$, and v_x shifted by $L_y \dot{\gamma}$. Furthermore, the x and z positions are always wrapped into the principal box due to the

periodic boundaries. This is the so-called Lees-Edwards boundary condition [26], which recovers the usual periodic boundary condition when $\dot{\gamma} = 0$. At equilibrium, it is isotropic in every direction. Therefore, once a wave vector $\mathbf{k}$ is selected, the two transversal directions are identical. However, at nonequilibrium with shear flow, the two transversal directions are anisotropic and need to be differentiated. Let us define $\mathbf{e}_x$, $\mathbf{e}_y$ and $\mathbf{e}_z$ as three unit vectors, which are along x, y, and z direction in the Cartesian coordinate, respectively. Thus, the mean profile of shear flow at steady state is characterized by $v_x = \dot{\gamma}y$ with $v_y = v_z = 0$. Suppose the initial wave vector is chosen as $\mathbf{k}_0 = k_x\mathbf{e}_x + k_y\mathbf{e}_y + k_z\mathbf{e}_z = (k_x, k_y, k_z)$. We define another three orthogonal unit vectors $\mathbf{e}_1$, $\mathbf{e}_2$ and $\mathbf{e}_3$ in such way that $\mathbf{e}_1$ is along $\mathbf{k}$ and $\mathbf{e}_{2,3}$ are perpendicular to $\mathbf{k}$,

$$\mathbf{e}_1 = \mathbf{k}_0/k_0, \tag{31}$$

$$\mathbf{e}_2 = [\mathbf{e}_y - (\mathbf{e}_1 \cdot \mathbf{e}_y)\mathbf{e}_1]/k_\perp, \tag{32}$$

$$\mathbf{e}_3 = \mathbf{e}_1 \times \mathbf{e}_2, \tag{33}$$

where $k_0 = |\mathbf{k}_0|$, $k_\perp = (k_x^2 + k_z^2)^{1/2}/k_0$ and $\mathbf{e}_y$ is taken as reference to define the first transversal direction $\mathbf{e}_2$. Note that subscript x, y, or z refers to the fixed Cartesian coordinate, while subscript 1, 2, or 3 refers to the wave vector coordinate.

By considering moderate shear rate $\dot{\gamma} \lesssim \nu k_0^2$, cross correlations may be neglected [25, 35, 36]. To account for the advection of the shear, let $\mathbf{k}(t) = (k_x, k_y - \dot{\gamma}tk_x, k_z)$ denote the time dependent wave vector and $k(t) = |\mathbf{k}(t)|$. Hence, the three unit wave vectors in Eqs. (31), (32), and (33) are time-dependent as well. The evolutions of the fluctuating variables in k-space can be solved via the perturbation theory [25] and therefore, the normalized transversal autocorrelation functions (TACFs) read as [36]

$$C_{T_1}(\mathbf{k}, t) = \frac{<\tilde{v}_2(\mathbf{k}, t)\tilde{v}_2(\mathbf{k}, 0)>}{<\tilde{v}_2^2(\mathbf{k}, 0)>}$$
$$= \left(\frac{k_0}{k(t)}\right)e^{-\nu\alpha(\mathbf{k}, t)}, \tag{34}$$

$$C_{T_2}(\mathbf{k}, t) = \frac{<\tilde{v}_3(\mathbf{k}, t)\tilde{v}_3(\mathbf{k}, 0)>}{<\tilde{v}_3^2(\mathbf{k}, 0)>}$$
$$= e^{-\nu\alpha(\mathbf{k}, t)}. \tag{35}$$

Here, $\tilde{v}_2$ and $\tilde{v}_3$ are the spatial Fourier transform of the two fluctuating velocity components along $\mathbf{e}_2$ and $\mathbf{e}_3$, respectively, which are perpendicular to the wave vector direction $\mathbf{e}_1$. Moreover, α is defined as

$$\alpha(\mathbf{k}, t) = k_0^2 t - \dot{\gamma}k_x k_y t^2 + \frac{1}{3}\dot{\gamma}^2 k_x^2 t^3. \tag{36}$$

It is simple to see that if $\dot{\gamma} = 0$, $\mathbf{k} = (k_x, k_y, k_z)$ and $\alpha(\mathbf{k}, t) = k^2 t$. Therefore, Eqs. (34) and (35) identical and degenerate to the solutions at equilibrium [13, 23, 24].

In particle simulations, we define the fluctuating velocity $\delta\mathbf{v}(\mathbf{x}, t) = (\delta v_x(\mathbf{x}, t), \delta v_y(\mathbf{x}, t), \delta v_z(\mathbf{x}, t))$ of a particle at location $\mathbf{x} : (x, y, z)$ and time instant t under simple shear flow, so

$$\delta v_x(\mathbf{x}, t) = v_x(\mathbf{x}, t) - \dot{\gamma}y,$$
$$\delta v_y(\mathbf{x}, t) = v_y(\mathbf{x}, t),$$
$$\delta v_z(\mathbf{x}, t) = v_z(\mathbf{x}, t). \tag{37}$$

The TACFs in k-space are calculated as

$$< \tilde{v}_\sigma(\mathbf{k}, t)\tilde{v}_\sigma(\mathbf{k}, t + \tau)>=$$
$$\frac{1}{N_s}\sum_{s=1}^{N_s}\tilde{v}_\sigma(\mathbf{k}, t)\tilde{v}_\sigma(\mathbf{k}, t + \tau), \tag{38}$$

where the transversal directions correspond to $\sigma = 2$ and 3 and N_s is the number of independent simulation runs. The Fourier transform in space is defined as

$$\tilde{f}(\mathbf{k}, \delta\mathbf{v}(\mathbf{x}, t)) = \frac{1}{N_p}\sum_{j=1}^{N_p}\delta\mathbf{v}(\mathbf{x}_j, t)e^{-i\mathbf{k}(t)\cdot\mathbf{x}_j(t)}, \tag{39}$$

$$\tilde{v}_\sigma(\mathbf{k}, t) = \tilde{f}(\mathbf{k}, \delta\mathbf{v}(\mathbf{x}, t)) \cdot \mathbf{e}_\sigma \tag{40}$$

where j is particle index and N_p is the number of particles in each simulation. Note that fluctuating velocities are projected on unit vectors in the wave vector coordinate via Eq. (40) after been transformed in Eq. (39).

At equilibrium, there is no time origin, therefore time averaging may be performed before ensemble averaging in Eq. (38) so that accurate statistics are obtained. At nonequilibrium, however, it is generally much more expensive to reduce the statistical errors of TACFs, due to the time dependence of $\mathbf{k}(t)$ and $\mathbf{e}_\sigma(t)$.

A. DPD simulations under shear flow with Lees-Edwards boundary condition

To verify the theory, we perform DPD simulations in a box of $[0, L_x] \times [-L_y/2, L_y/2] \times [0, L_z]$ so that the mean velocity $v_x = \dot{\gamma}y$ is consistent with the theory. Periodic boundary conditions are applied in x and z directions while along the shear gradient in y direction we apply the Lees-Edwards boundary condition. In practice, we utilize an implementation of the deforming triclinic box [37] for the Lees-Edwards boundary condition. In molecular dynamics, it is the so-called SLLOD dynamics for the canonical ensemble [38]. The technical difference is that DPD has a built-in pairwise thermostat while MD relies on various classical thermostats, such as the Nóse-Hoover thermostat. Input parameters and properties of DPD fluids are the same as given in Section II A. $L_x = L_y = L_z = 10$.

1. Wave vector perpendicular to the shear plane: $\mathbf{k}_0 = (0, 0, k_z)$

If we take the initial wave vector $\mathbf{k}_0 = (0, 0, 2\pi/L_z)$, then $\mathbf{k}(t) \equiv \mathbf{k}_0$. Therefore, the two transversal directions
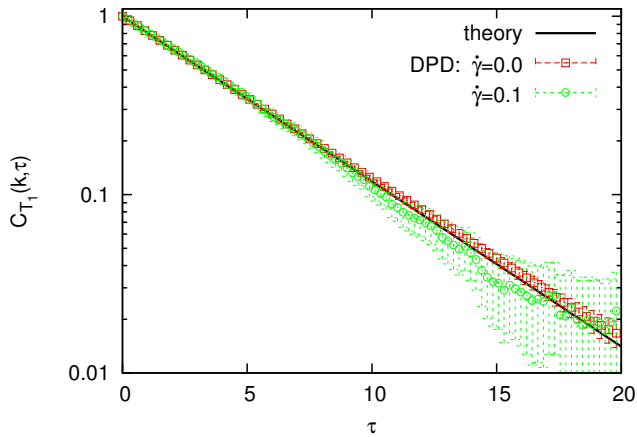
FIG. 4: (Color online) Transversal autocorrelation function in logarithmic-linear scale: $\mathbf{k}_0 = (0, 0, 2\pi/L_z)$ for $\dot{\gamma} = 0$ and 0.1. Error bars for $\dot{\gamma} = 0$ indicate standard error of 200 independent simulations while for $\dot{\gamma} = 0.1$ of 10000 independent simulations.

are isotropic and the same as in equilibrium. The shear rate is taken as $\dot{\gamma} = 0.1$. Results of the simulations are compared with the theory for the first transversal direction in Fig. 4. Although the time origin for $\dot{\gamma} = 0.1$ is the same for this particular wave vector, we treat the time origin differently when performing the post-processing just as for a general wave vector. Therefore, we perform only ensemble averaging and the error bar for $\dot{\gamma} = 0.1$ is relative larger.

It is evident that the TACFs for equilibrium and nonequilibrium are equivalent, when the wave vector $\mathbf{k}(t)$ is along the z direction. The other TACFs are the same and hence we do not show the results here.

2. Wave vector in the shear plane: $\mathbf{k}_0 = (k_x, 0, 0)$

If we take the initial wave vector $\mathbf{k}_0 = (2\pi/L_x, 0, 0)$, then $\mathbf{k}(t) = (2\pi/L_x, -\dot{\gamma}t2\pi/L_x, 0)$ becomes a time-dependent two-dimensional vector to account for the advection of the shear flow. Therefore, the two TACFs in Eqs. (34) and (35) are anisotropic. The shear rate is again taken as $\dot{\gamma} = 0.1$. Results of the simulations are compared with the theory for the two transversal directions in Fig. 5, where overall good agreement is observed. In this case, the decaying exponent is $\alpha(\mathbf{k}, t) = k_0^2 t + \dot{\gamma}^2 k_x^2 t^3/3$. Therefore, the TACFs of nonequilibrium shear flow signify the equilibrium behavior $\alpha(\mathbf{k}, t) \sim k_0^2 t$ at short time whereas they show a more advective behavior $\alpha(\mathbf{k}, t) \sim \dot{\gamma}^2 k_x^2 t^3/3$ at long time. We note the two different intercepts with time axis on the two plots of Fig. 5, which indicates a stronger decay for the first transversal direction due to the $k_0/k(t)$ term in Eq. (34). We note again that both time and ensemble averaging are performed for the equilibrium case, whereas only ensem-
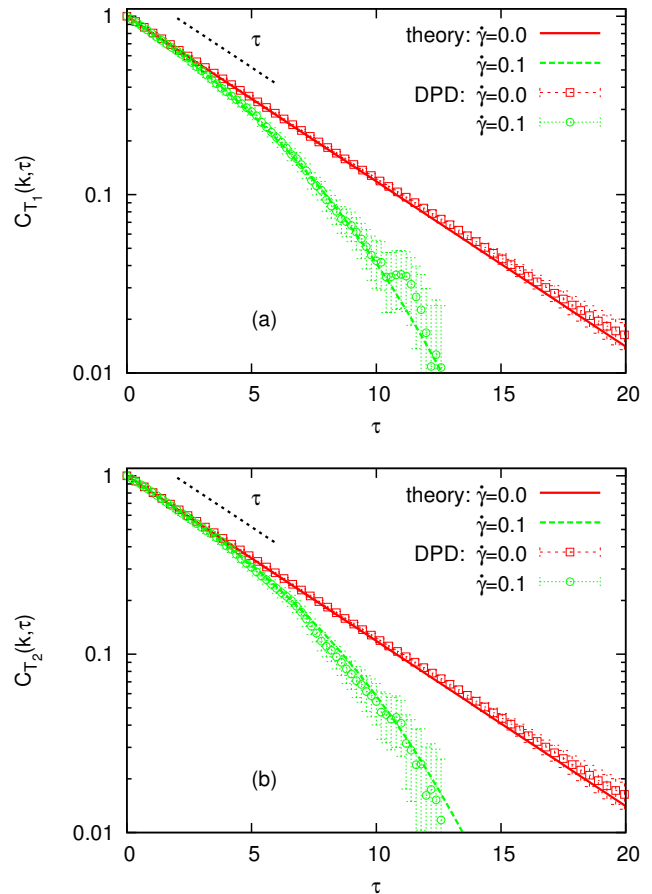

FIG. 5: (Color online) Transversal autocorrelation functions in logarithmic-linear scale: $\mathbf{k}_0 = (2\pi/L_x, 0, 0)$ for $\dot{\gamma} = 0$ and 0.1. (a) δv_y and $\mathbf{e}_2 = \mathbf{e}_y$. (b) δv_z and $\mathbf{e}_3 = \mathbf{e}_z$. Error bars for $\dot{\gamma} = 0$ indicate standard error of 200 independent simulations while for $\dot{\gamma} = 0.1$ of 10000 independent simulations.

ble averaging is performed for the nonequilibrium case. Therefore, the error bar for $\dot{\gamma} = 0.1$ is relative larger.

B. Hybrid simulations of wall-bounded shear flow

Since we are primarily interested in the fluctuations of hybrid simulations, we re-examine the hybrid simulations in Section II D and focus on the fluctuating velocities in the shear flow at steady state.

If there is any artifact on the fluctuations in the hybrid simulations, it must be most evident in the vicinity of the interface region. Therefore, we select to examine region Γ_e with $2r_c$ thickness slab just below the hybrid reference line y_r. The examined region ranges in $[0, L_x]$ and $[0, L_z]$ in the other two periodic directions, respectively. For reference of the "true fluctuations", we run full DPD simulations in a box of $[0, 10] \times [0, 30] \times [0, 10]$, which covers the whole domain of the hybrid simulations,
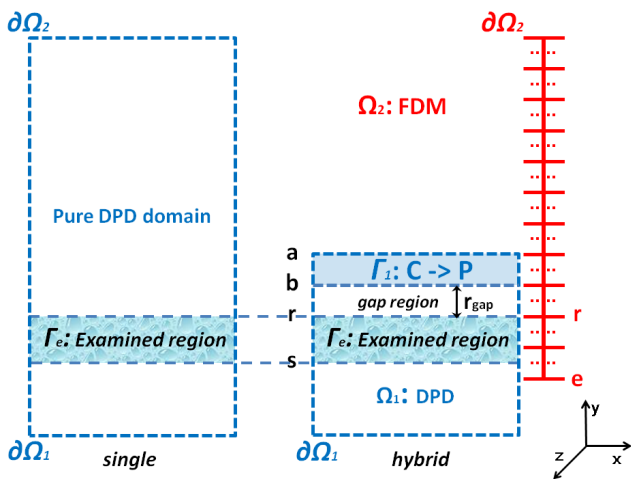
FIG. 6: (Color online) Sketch for a full particle simulation versus a hybrid particle-continuum simulation in wall-bounded shear flow. Left: full DPD simulation in the whole domain. Right: hybrid simulation of concurrent coupling between DPD and FDM. To reduce the errors in thermal fluctuations, a gap region is introduced between the artificial boundary Γ_1 and the interior: $y_b - y_r = r_{gap}$. The fluctuations in the shadowed regions Γ_e with thickness $2r_c$ adjacent to the hybrid reference line y_r are examined and compared with each other.

as sketched in Fig. 6. Fluctuations in the two geographically identical regions Γ_e are compared with each other.

As seen earlier, the wave vector $\mathbf{k}(t)$ is time-dependent to account for the shear flow. If we take an initial wave vector with component $k_x \neq 0$ or $k_y \neq 0$, then $k_y(t) = k_y - \dot{\gamma} t k_x \neq 0$ for an arbitrary t. However, the wall bounded shear flow considered in Section II D does not allow for a straightforward Fourier transform with periodic basis in the y direction. Therefore, we focus only on the initial wave vectors $\mathbf{k}_0^{n_w} = (0, 0, 2n_w\pi/L_z)$. As the constraint dynamics in Γ_1 is performed in the x direction, we will focus on the fluctuating velocity component δv_x, which is along the second transversal direction $\mathbf{e}_3 = \mathbf{e}_x$.

1. Errors in hydrodynamic fluctuations

The TACFs of hybrid simulations with Maxwell buffer and least constraint dynamics are compared with those of full particle simulations in Fig. 7. The time axis is rescaled with νk^2 so that results of different wave numbers may be compared as well. We observe that if Γ_1 is placed just adjacent to the examined region Γ_e, the TACFs of hybrid simulations deviate significantly from the reference results taken from the full particle simulations. This indicates a large error in the fluctuations in Γ_e from the hybrid simulations. With Γ_1 moving away from Γ_e, the error decreases monotonically with

r_{gap}. In particular, the artificial disturbances from the Maxwell buffer are more pronounced than those from the least constraint dynamics in two different length scales L_z and $L_z/2$, corresponding to $\mathbf{k}_0^1 = (0, 0, 2\pi/L_z)$ and $\mathbf{k}_0^2 = (0, 0, 4\pi/L_z)$, respectively. The relaxation dynamics and flux imposition have very similar effects as the least constraint dynamics, therefore the results are not shown.

To quantify the errors in the fluctuations, we define the root mean squared error (RMSE) for the TACFs of the hybrid simulations from that of the full particle simulations as

$$RMSE = \sqrt{\sum_i^{N_\tau} \left[C_{T_2}^h(\mathbf{k}, \tau_i) - C_{T_2}^f(\mathbf{k}, \tau_i) \right]^2 / N_\tau}, \quad (41)$$

where $C_{T_2}^h(\mathbf{k}, \tau)$ is from the hybrid simulations, $C_{T_2}^f(\mathbf{k}, \tau)$ is from the full particle simulations, and N_τ is the number of discrete time steps. Results of RMSE for the four different constraint dynamics methods are summarized in Fig. 8. If Γ_1 is placed adjacent to Γ_e. the Maxwell buffer induces higher errors than the other three methods in both length scales represented by $\mathbf{k}_0^1$ and $\mathbf{k}_0^2$. If Γ_1 is placed further away from Γ_e, that is, $r_{gap} \geq 2r_c$, all four methods have very similar performance and the errors seem to decay linearly with r_{gap}.

2. Identification of sources of errors

If we recall the operations described in Section II C for the particle simulations in the truncated subdomain, there are potentially two sources of artifacts. The first source is associated with the truncation itself (see line y_a in Fig. 1), as a mean pressure and specular reflection are needed to retain particles in the subdomain. The second source is associated with the constraint dynamics operated in the artificial boundary Γ_1. When we try to reduce the errors in the fluctuations in Section III B 1, we move Γ_1 away from the examined region Γ_e. In fact, this moves both sources of artifacts together away from Γ_e. To explicitly identify each source of artifacts, we wish to move the truncation line independently from the artificial boundary Γ_1. Therefore, we detach the truncation line $y_{a'}$ from the upper edge y_a of Γ_1 and $y_{a'} - y_a = r_{det}$, as sketched in Fig. 9. The DPD particles between y_a and $y_{a'}$ are coupled indirectly with FDM only through their interactions with particles within Γ_1.

For $r_{gap} = 0$, we calculate the RMSE for fluctuations of hybrid simulations with truncation line $y_{a'}$ at various positions ($r_{det} \geq 0$). Effects of truncation alone on the errors of fluctuations are compared with effects from both the truncation and the constraint dynamics in Fig. 10. Moving away the truncation line $y_{a'}$ or increasing r_{det} simply reduces the error of the truncation while exposing more clearly the error of the constraint dynamics. We observe that the dominating source of artifacts
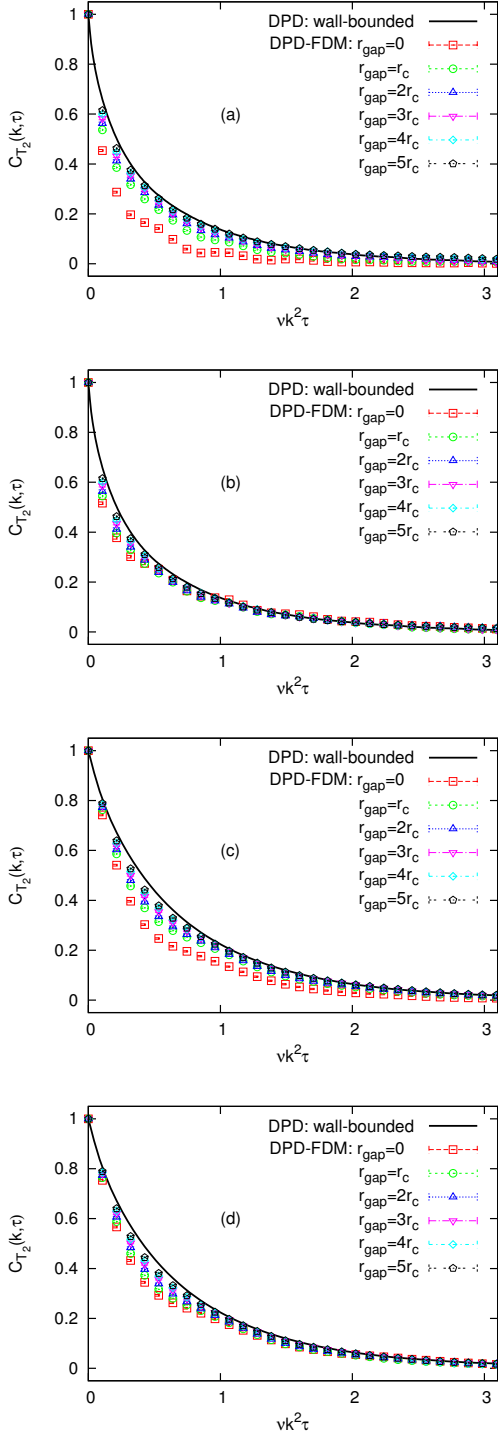
FIG. 7: (Color online) Transversal autocorrelation functions of hybrid simulations. (a) Maxwell buffer with wave vector $\mathbf{k}_0^1 = (0, 0, 2\pi/L_z)$. (b) Least constraint dynamics with wave vector $\mathbf{k}_0^1 = (0, 0, 2\pi/L_z)$. (c) Maxwell buffer with wave vector $\mathbf{k}_0^2 = (0, 0, 4\pi/L_z)$. (d) Least constraint dynamics with wave vector $\mathbf{k}_0^2 = (0, 0, 4\pi/L_z)$.
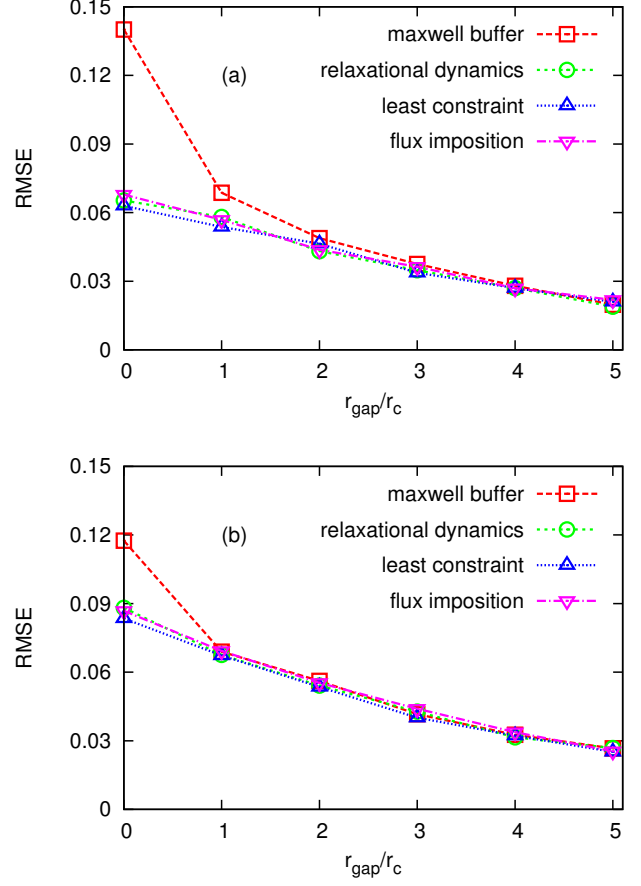

FIG. 8: (Color online) Root mean square error (RMSE) for the transversal autocorrelation functions of hybrid simulations versus r_{gap}. (a) Wave vector $\mathbf{k}_0^1 = (0, 0, 2\pi/L_z)$. (b) Wave vector $\mathbf{k}_0^2 = (0, 0, 4\pi/L_z)$.
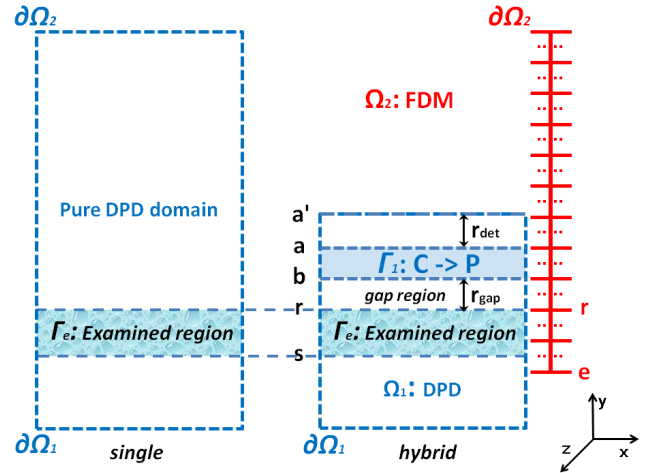
FIG. 9: (Color online) The same sketch as in Fig. 6 except that the truncation line $y = y_{a'}$ of the particle subdomain is detached from the artificial boundary $\Gamma_1 : [y_b, y_a]$. $y_{a'} - y_a = r_{det}$.
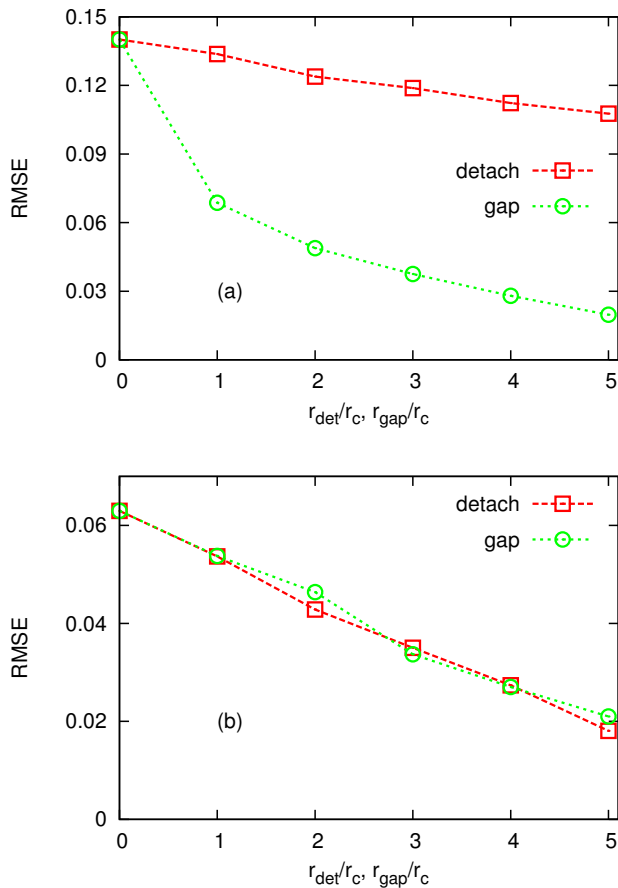
FIG. 10: (Color online) Root mean square error (RMSE) for the transversal autocorrelation functions of hybrid simulations: errors from constraint dynamics alone versus errors from both truncation and constraint dynamics. (a) Maxwell buffer with wave vector $\mathbf{k}_0^1 = (0, 0, 2\pi/L_z)$. (b) Least constraint dynamics with wave vector $\mathbf{k}_0^1 = (0, 0, 2\pi/L_z)$. Results of "gap" are the same as those in Fig. 8.

with Maxwell buffer is from the constraint dynamics itself. For the least constraint dynamics, the error comes almost solely from the truncation effects. The results from the relaxation dynamics are similar to that of the least constraint dynamics, therefore are not shown.

IV. CONCLUSION

By employing the framework of domain decomposition method (DDM), we study the concurrent coupling of heterogeneous fluid solvers in two overlapping subdomains. In particular, one solver is deterministic and operates at the continuum level. We adopt the finite difference method (FDM) as a representative of this class of solvers. The other solver is stochastic and applied at the mesoscopic level. We utilize the dissipative particle dynamics

(DPD) method as a representative of this class of solvers. With time advancing, each solver integrates the dynamics in its own subdomain and updates the other solver's artificial boundary within the overlapping region. This procedure proceeds alternatively until the end of the hybrid simulation. The global solution is pieced together from the two solvers at a hybrid reference line y_r chosen arbitrarily within the overlapping region. Once y_r is selected, it is fixed so that other spatial parameters may be varied to study their effects on the results.

At each communication step Δt, to impose the artificial boundary Γ_2 of the continuum solver, we simply perform spatial-temporal-averaging on state variables in the neighboring region of the particle simulation over Δt and utilize the mean $(P \rightarrow C)$. It is not simple to impose the artificial boundary Γ_1 of the particle simulation, due to the stochasticity of the particle dynamics. In general, a constraint dynamics is performed within Γ_1 in such a way that the averaged state variable resembles the continuum at the same region $(C \rightarrow P)$ and thermal fluctuations are altered minimally. In this sense, Γ_1 is a "stochastic Dirichlet boundary" that has fluctuations around a given mean value. However, there has been no consensus over different strategies of implementing the constraint dynamics. Therefore, we select four popular methods of the constraint dynamics for testing. All four methods are widely adopted in particle dynamics in the context of hybrid simulations, and they all deliver the targeted mean flows accurately.

Due to both the truncation of the subdomain and the constraint dynamics performed in the artificial boundary Γ_1, the errors in hydrodynamic fluctuations in the subdomain of particle simulation are unavoidable. To this end, we focus on a simple shear flow and resort to the autocorrelation functions (ACFs) of the fluctuating state variables in k-space to quantify the fluctuation errors. From the solutions of linearized fluctuating hydrodynamics, we know that the ACFs encode the generation, transport and dissipation of the fluctuations. Moreover, with different wavenumbers, the results indicate the collective behavior of particles at different length scales. Therefore, the quantity of interest is the ACF of an examined region Γ_e in the interior. Furthermore, we select Γ_e to be adjacent to the hybrid reference line y_r. The errors of fluctuations in other regions further away from y_r are expected to be weaker than that of Γ_e. In the simple shear flow with flow direction in x and velocity gradient in y, the constraint dynamics is performed along x, therefore we focus on the velocity fluctuations δv_x. We take initial wave vectors $\mathbf{k}_0^{n_w} = (0, 0, 2n_w\pi/L_z)$ along the vorticity direction (z), which is periodic and time invariant. Hence, the velocity fluctuations δv_x are transversal to the wave vectors. At steady state of the flow, the transversal ACF or TACF is calculated after δv_x in Γ_e are transformed in k-space. Finally, the TACFs of hybrid simulations with the four different constraint dynamics are compared with that of full particle simulations performed in the whole domain.

We observed *two sources* of errors in thermal fluctuations and further quantified the errors. The first one is associated with the *truncation* of the subdomain for particle simulations. More specifically, the mean pressure and specular reflection applied at the end of the truncated side lead to disturbances of hydrodynamic fluctuations. The second source is associated with the *constraint dynamics* performed within the artificial boundary Γ_1, which introduces potential intrusions to the hydrodynamic fluctuations. If the sources of the errors are moved away from the examined region, both types of errors may be reduced, but only slowly with a linear dependence on the distance. For each of the four constraint dynamics methods implemented in Γ_1, we further elaborate on the two sources of errors.

For the Maxwell buffer with a local equilibrium assumption, the constraint dynamics is achieved by randomizing the velocity completely in Γ_1 at each δt according to the Maxwell-Boltzmann distribution. For a fixed temperature, the distribution is centered at a given mean value from the continuum solver. Therefore, the truncation effect is almost completely masked by the randomization of velocity. This can be proven by moving the artificial boundary Γ_1 or the truncated line separately. Moving away the Γ_1 reduces the error much more significantly than moving the truncated line alone, as seen in Fig. 10(a).

The constraint dynamics by the least constraint and relaxation are essentially very similar and the only difference is on the technical aspect. The relaxation dynamics has a parameter ϵ to be tuned so that it performs as well as the least constraint dynamics for a target mean flow. This tuning leads to difficulties in practice, as ϵ may depend on both the dynamic properties of the particles and the flow conditions. In this sense, the least constraint dynamics is straightforward and more practical. Both the least constraint and relaxation dynamics generate negligible errors in the fluctuations. The dominating errors come almost solely from the truncation effects, that is, moving away the truncated line alone reduces error just as effectively as moving away the entire artificial boundary Γ_1, as seen from Fig. 10(b).

For the constraint dynamics via imposition of flux, effects from truncation and constraint dynamics cannot be separated, as both the truncation operations (mean pressure and specular reflection) and flux imposition are bounded to the position of the truncated line.

From the perspective of computational efficiency, there is no difference between moving the truncation line alone and moving the entire artificial boundary Γ_1 away from the examined region Γ_e. To reduce the errors in hydrodynamic fluctuations, simply moving the entire Γ_1 away from the interior (e.g., Γ_e) is a more convenient implementation and the error of fluctuations may be quantified solely by one length-scale parameter r_{gap} between Γ_1 and Γ_e. For a small r_{gap}, the Maxwell buffer has the most erroneous influence on the fluctuations, while the other three methods of constraint dynamics have similar effects.

We may understand the relative worse performance of Maxwell buffer by considering the iso-surface of constant temperature in the phase space of particles in Γ_1. The Maxwell buffer simply picks up a random phase point at every δt, which is very abrupt and discontinuous. In contrast, the operations of the other three methods are gentle and close to moving the phase point smoothly on the iso-surface. From another perspective, the Maxwell buffer does not consider any inherent fluctuations, therefore it tends to decorrelate their correlations and causes artificial dissipation of the system. Nevertheless, for $r_{gap} \geq 2r_c$, disturbances from local operations of any constraint dynamics in Γ_1 fade away and all four methods have similar effects, that is, the errors decrease linearly as r_{gap}. It may be possible to avoid the errors in fluctuations due to the truncation effects of the particle subdomain. For example, by adopting a proper particle deletion-insertion strategy, a more accurate grand canonical ensemble in the particle subdomain may be recovered.

Appendix A: Forces on a particle near a planar interface in DPD

When a particle is near a planar interface, there is no full-spherical support for the calculation of interacting forces between particles. In this work, the interface is either between the fluid and a solid wall or at the truncation line of the particle subdomain in the context of hybrid simulation. We follow Refs. [5, 31] to compute an integral force, to compensate any "missing force" from the exterior. The integral force is based on the continuum assumption and is an averaged force.
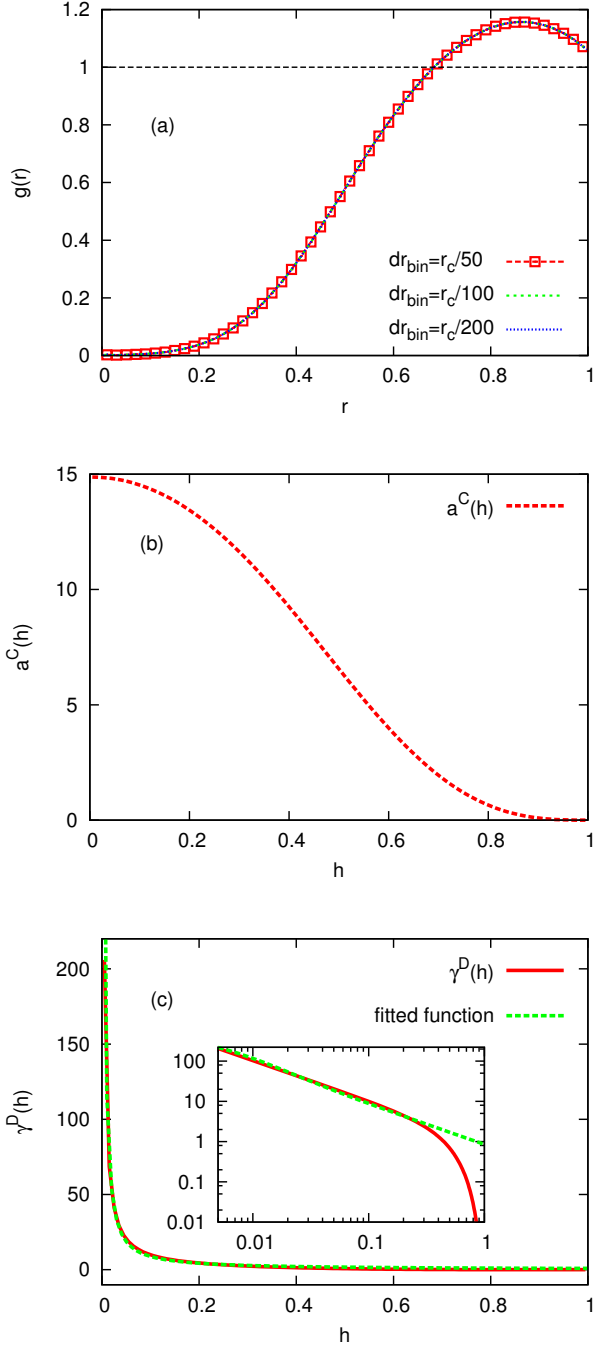
FIG. 11: (Color online) Radial distribution function and boundary integral forces as functions of distance to a planar interface: $r_c = 1.0$ and $n = 3$. (a) Radial distribution function. (b) Conservative force. (c) dissipative force.

For the conservative force from the exterior, it is calculated as [5, 31]

$$\mathbf{F}_{ave}^C(h_i) = \sum_{j \in ext} \mathbf{F}_{ij}^C$$
$$\approx n \int_{ext} \mathbf{F}^C(r) g(r) dv = \pm a^C(h_i)\mathbf{e}_y, \quad \text{(A1)}$$

where $g(r)$ is the radial distribution function of particles and can be calculated in a separate simulation at equilibrium. The integration is performed only on the exterior part of a spherical volume. In addition, we assume the interface is perpendicular to y direction. Due to symmetry, $\mathbf{F}_{ave}^C(h_i)$ is along y direction inwards to the interior fluid. Given the input parameters in Section II A, the $g(r)$ of DPD particles is shown in Fig. 11(a), where results are not sensitive to the bin-size of averaging. According to Eq. (A1), the numerical values of $a^C(h)$ are plotted as a function of distance h to the interface in Fig. 11(b). $\mathbf{F}_{ave}^C(h_i)$ is applied to any particle i with $h_i < r_c$ away from a planar interface.

Similarly, for the dissipative force from the exterior, if we assume a locally shear flow in x direction, it is calculated as [31]

$$\mathbf{F}_{ave}^D(h_i) = \sum_{j \in ext} \mathbf{F}_{ij}^D$$
$$\approx n \int_{ext} \mathbf{F}^D(r) g(r) dv = \pm \gamma^D(h_i)\mathbf{e}_x. \quad \text{(A2)}$$

The numerical values of $\gamma^D(h)$ are plotted in Fig. 11(c) and they may be fitted as a function [31],

$$\gamma^D(h) = C_1(h + \delta h)^{-1} + C_2(h + \delta h)^{-2}$$
$$+ C_3(h + \delta h)^{-3}, \quad \text{(A3)}$$

where $C_1 = 0.8504$, $C_2 = 9.6 \times 10^{-3}$, $C_3 = 4.0 \times 10^{-4}$, and $\delta h = 0.01$. Note that the fitted function is slightly different from the actual numerical values at large distance. We will simply utilize the numerical values with the largest value at $h = 0.01$ directly in this work. Due to the strong conservative force at short distance, it is improbable for particles to have $h < 0.01$.

$\mathbf{F}_{ave}^D(h_i)$ is applied only to particle i with $h_i < r_c$ away from a planar solid wall. Accordingly, a random force $\mathbf{F}_{ave}^R(h_i) = \theta_i \sqrt{2k_B T \gamma^D(h_i)}\mathbf{e}_x$ is also applied to the same particle, where θ_i is a Gaussian white noise.

Given the input parameters in Section II A, we run a simple wall-bounded Couette flow and plot the velocity, density and temperature in Fig. 12, where results agree with the theory and recover the previous work [31] very well.

We note that in the context of hybrid simulation, particles with distance $h_i < r_c$ away from the truncation line of the particle subdomain are *not* subject to $\mathbf{F}_{ave}^D(h_i)$ or $\mathbf{F}_{ave}^R(h_i)$, and their dynamics are according to the constraint dynamics described in Section II C.
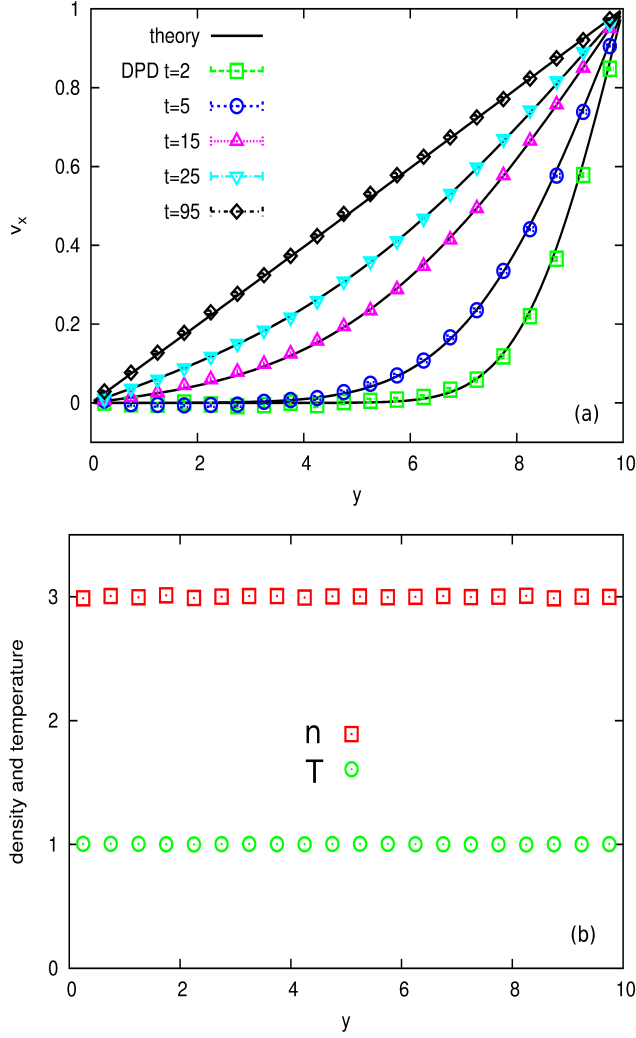
FIG. 12: (Color online) Mean profiles for transient Couette flow: $L_y = 10$, $\dot{\gamma} = 0.1$, $v_w = \dot{\gamma}L_y = 1.0$, and $Re = v_w L_y/\nu = 18.52$. (a) Velocity. (b) Density and temperature.

[1] S. T. O'Connell and P. A. Thompson, Phys. Rev. E **52**, R5792 (1995).
[2] N. G. Hadjiconstantinou and A. T. Patera, International Journal of Modern Physics C **08**, 967 (1997).
[3] E. G. Flekkøy, G. Wagner, and J. Feder, Europhys. Lett. **52**, 271 (2000).
[4] X. B. Nie, S. Y. Chen, W. N. E, and M. O. Robbins, J. Fluid Mech. **500**, 55 (2004).
[5] T. Werder, J. H. Walther, and P. Koumoutsakos, J. Comput. Phys. **205**, 373 (2005).
[6] W. Ren and W. E, J. Comput. Phys. **204**, 1 (2005).
[7] M. Praprotnik, L. Delle Site, and K. Kremer, J. Chem. Phys. **123**, 224106 (2005).
[8] R. Delgado-Buscalioni and G. De Fabritiis, Phys. Rev. E **76**, 036709 (2007).
[9] D. A. Fedosov and G. E. Karniadakis, J. Comput. Phys.
[10] M. K. Borg, D. A. Lockerby, and J. M. Reese, Journal of Computational Physics **233**, 400 (2013).
[11] X. Bian, Z. Li, and G. E. Karniadakis, J. Comput. Phys. **297**, 132 (2015).
[12] Y.-H. Tang, S. Kudo, X. Bian, Z. Li, and G. E. Karniadakis, J. Comput. Phys. **297**, 13 (2015).
[13] X. Bian, Z. Li, M. Deng, and G. E. Karniadakis, Phys. Rev. E **92**, 053302 (2015).
[14] P. Neumann, H. Flohr, P. Jarmatz, N. Tchipev, and H.-J. Bungartz, Computer Physics Communications (2015).
[15] B. Smith, P. Bjorstad, and W. Gropp, *Domain decomposition: parallel multilevel methods for elliptic partial differential equations* (Cambridge University Press, 1996).
[16] W. Pan, B. Caswell, and G. E. Karniadakis, Langmuir **26**, 133 (2009).
228, 1157 (2009).

[17] X. Bian, S. Litvinov, R. Qian, M. Ellero, and N. A. Adams, Phys. Fluids **24**, 012002 (2012).

[18] A. Vázquez-Quesada, M. Ellero, and P. Español, Microfluid Nanofluidics **13**, 249 (2012).

[19] D. A. Fedosov, A. Sengupta, and G. Gompper, Soft Matter **11**, 6703 (2015).

[20] S. Litvinov, M. Ellero, X. Y. Hu, and N. A. Adams, Phys. Rev. E **77**, 066703 (2008).

[21] H. Lei and G. E. Karniadakis, Proc. Natl. Acad. Sci. USA (2013).

[22] X. Li, Y.-H. Tang, H. Liang, and G. E. Karniadakis, Chem. Commun. **50**, 8306 (2014).

[23] J. P. Boon and S. Yip, *Molecular Hydrodynamics* (Dover Publications, Inc., New York, 1991).

[24] J. P. Hansen and I. R. McDonald, *Theory of simple liquids*, 4th ed. (Elsevier, 2013).

[25] J. Lutsko and J. W. Dufty, Phys. Rev. A **32**, 3040 (1985).

[26] A. W. Lees and S. F. Edwards, J. Phys. C: Solid State Phys. **5**, 1921 (1972).

[27] P. J. Hoogerbrugge and J. M. V. A. Koelman, Europhys. Lett. **19**, 155 (1992).

[28] P. Español and P. Warren, Europhys. Lett. **30**, 191 (1995).

[29] R. D. Groot and P. B. Warren, J. Chem. Phys. **107**, 4423 (1997).

[30] X. Fan, N. Phan-Thien, S. Chen, X. Wu, and T. Y. Ng, J. Chem. Phys. **18**, 063102 (2006).

[31] H. Lei, D. A. Fedosov, and G. E. Karniadakis, J. Comput. Phys. **230**, 3765 (2011).

[32] W. Ren, J. Comput. Phys. **227**, 1353 (2007).

[33] Z. Li, A. Yazdani, A. Tartakovsky, and G. E. Karniadakis, The Journal of Chemical Physics **143**, 014101 (2015).

[34] H. Goldstein, C. Poole, and J. Safko, *Classical Mechanics*, 3rd ed. (Addison Wesley, 2001).

[35] M. Otsuki and H. Hayakawa, J. Stat. Phys.: Theory and Experiment **2009**, L08003 (2009).

[36] A. Varghese, C. Huang, R. G. Winkler, and G. Gompper, Phys. Rev. E **92**, 053002 (2015).

[37] S. Plimpton, J. Comput. Phys. **117**, 1 (1995).

[38] D. J. Evans and G. Morriss, *Statistical Mechanics of nonequilibrium liquids*, 2nd ed. (Cambridge University Press, 2008).